Three-Dimensional Simulations of Plume-Lithosphere Interaction at the Hawaiian Swell

William B. Moore,* Gerald Schubert, Paul Tackley

Rapid lithospheric thinning by mantle plumes has not been achieved in numerical experiments performed to date. Efficient thinning depends on small-scale instabilities that convectively remove lithospheric material. These instabilities are favored by hotter plumes or stronger temperature dependence of viscosity, and a simple scaling independent of rheology controls their onset. This scaling allows extrapolation of the results of numerical experiments to the Earth's mantle. Mantle plumes between 100 and 150 kelvins hotter than the background mantle should exhibit small-scale convective rolls aligned with the plate motion. The unusual variation in heat flow across the Hawaiian swell may be due to such instabilities. It was found that the spreading of the plume creates a downwelling curtain of material that isolates it from the rest of the mantle for distances of at least 1000 kilometers from the plume origin. This isolation has important consequences for the geochemical heterogeneity of the lithosphere and upper mantle.

The Hawaiian Islands are part of a chain of massive volcanoes known collectively as the Hawaiian-Emperor seamount chain. They formed, one by one, as the Pacific lithospheric plate moved over a region of hot upwelling mantle called a hot spot. After passing over the hot spot, the islands gradually sank beneath the waves, forming atolls and completely submerged seamounts. The orderly conductive cooling and subsidence of the oceanic lithosphere as it ages and moves away from the mid-ocean ridge are disrupted around the hot spot, where the sea floor around the volcanoes is abnormally shallow (more than a kilometer shallower than normal 80- to 100-million-year–old sea floor) for hundreds of kilometers on either side of the chain (*1*). This broad uplift is known as the Hawaiian swell and, like the volcanism, is also a consequence of the passage of the lithosphere over the hot spot. It subsides slowly, and after about 30 million years, it is indistinguishable from normal sea floor.

The first attempts at explaining the behavior of the lithosphere at the Hawaiian swell drew on the analogy between the normal subsidence of the ocean floor and the gradual sinking of the swell and volcanic islands and hypothesized that the lithosphere's internal clock had been reset, making it behave as if it were 50 million years younger (*2*–*4*). This idea became known as lithospheric "rejuvenation" and has been hotly debated ever since.

The concept has been supported by the measured subsidence of the islands and the observation from geoid height anomalies that the swell was supported (compensated) by low-density material only 75 km beneath the sea floor (*4*), which is much shallower than the expected 100 to 125 km to the base of the oceanic lithosphere. This shallow, low-density material seemed to indicate that the lithospheric clock had indeed been reversed in the vicinity of the swell and that the lithosphere was being thinned.

A criticism of rejuvenation has stemmed from the 80-million-year age for the Pacific lithosphere at Hawaii, which requires a similar amount of time for conductive reheating. Subsequent models of the thermal response of the oceanic lithosphere to a sudden increase in heat flow or asthenospheric (shallow mantle) temperature (*2*, *5*, *6*) have demonstrated the critical role of upward advection of the lithosphere-asthenosphere boundary, most likely through small-scale convective instabilities (*6*, *7*), in overcoming this constraint. Such instabilities have been demonstrated in laboratory studies of thermal plumes (*8*) and cooling boundary layers (*9*, *10*). The latter studies revealed that such instabilities obey the scaling laws derived from boundary layer theory of convection in temperature-dependent viscosity fluids (*11*). This finding will prove useful in the analysis of the numerical results presented here.

Thermal models of the swell were at first supported by heat flow measurements along the swell (*12*), which showed a large increase as one moved along the swell. The later measurements (*13*) showed only a mild heat flow increase across the swell, with large variations. Although only sparsely sampled, these results were difficult to explain with thermal models of swell formation that predicted substantial lithospheric thinning and high heat flow downstream of the hot spot. Alternatives to rejuvenation emerged, which suggested that thermal perturbations to the lithosphere were small and that the swell was due to the spreading of a buoyant body of plume material within the asthenosphere that lies beneath the lithosphere (*14*). Although at odds with the observed compensation depth of the swell, these models did not require large heat flow downstream of the hot spot and were supported by seismic wave observations that indicated limited changes to the seismic velocities within the lithosphere (*15*) and numerical calculations of mantle flow that failed to produce substantial lithospheric thinning (*16*, *17*). Because the indications of lithospheric thinning seem contradictory, we undertook a new series of three-dimensional (3D) numerical experiments that investigated the interaction of a hot mantle upwelling or plume with the lithosphere.

The equations of mass, momentum, and energy conservation in an infinite–Prandtl number Boussinesq fluid were solved numerically in three dimensions by finite volume discretization on a staggered grid with STAG3D (*18*). Our model domain is a Cartesian box 400 km deep, extending 1600 km in the direction of plate motion and 800 km in the perpendicular direction (Fig. 1). There is a plane of mirror symmetry on one side, so that the plume is symmetric about the direction of plate motion. The lithosphere (shaded in Fig. 1) was forced across the box at the velocity of the Pacific plate (100 mm year^{-1}) applied at the top, whereas material could flow freely in or out of the sides. Vertical fluid flow was allowed at the bottom of the box, and stress-free boundary conditions were applied at the sides. A conductive thermal profile appropriate for 80-million-year-old lithosphere was advected in from the upstream boundary and was swept across the hot spot, which was modeled as a fixed hot patch at the base of the

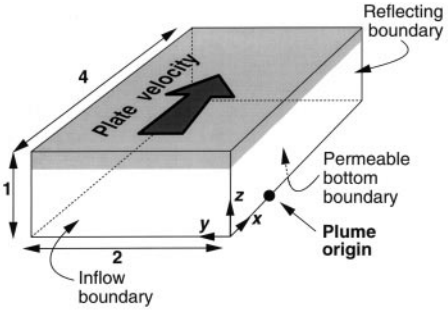

Fig. 1. The computational domain for models of a plume interacting with a moving plate. The shaded portion represents the lithosphere.

W. B. Moore and P. J. Tackley, Department of Earth and Space Sciences, University of California, Los Angeles, 3806 Geology Building, Los Angeles, CA 90095–1567, USA.
G. Schubert, Department of Earth and Space Sciences and Institute of Geophysics and Planetary Physics, University of California, Los Angeles, CA 90095–1567, USA.
*To whom correspondence should be addressed.

domain with a Gaussian temperature profile with a 67-km half-width and a peak temperature T_p above that of the background mantle. We varied T_p in our experiments but left the plume width fixed. These values resulted in varying buoyancy flux through the hot patch that should be compared with the 6 to 8 $\times$ 10^3 kg s^{-1} flux estimated for the Hawaiian swell (*19*).

The chief disadvantage of limiting the depth of the computational domain is that deeper flow is not accounted for and thus topography and geoid at the upper surface are not reliably determined at scales larger than the depth of the domain (400 km). This flow can be partially accounted for at the risk of introducing some model dependence on the bottom boundary condition (*17*). Instead, only qualitative topography and geoid comparisons were made between the results of our models and the Hawaiian swell. The topography and geoid are not particularly strong constraints on the flow beneath the lithosphere in any case, because they are very sensitive to the poorly known viscosity structure of the mantle (*20*).

A Newtonian viscosity law based on the homologous temperature (ratio of the temperature to the solidus temperature) given by

$$\eta = \eta_0 \exp\left(A\frac{T_m}{T}\right) \quad (1)$$

was used, where η_0 and A are scaling constants, T is temperature, and T_m is the solidus temperature given by

$$T_m = 1400 + 4.38z - 5.08 \times 10^{-3}z^2 \quad (2)$$

where z is the depth in kilometers and T_m is given in kelvins. This solidus was derived from the best fitting quadratic function of depth to the solidus of anhydrous peridotite (*21*) for pressures below 15 GPa. The extreme temperature dependence of this rheological law leads to numerical difficulties at large values of A. One way to avoid such problems is to impose a viscosity cutoff, so that the very cold regions of the domain do not overwhelm the numerical method. Alternatively, the very coldest portions of the lithosphere can be left out of the domain, and the surface temperature can be raised. We chose the latter approach, using an effective surface temperature of 800 K, so that we could use values of A up to 15. The top of the box, therefore, can be considered as a horizontal 800-K isotherm above which the lithosphere is cold enough to behave rigidly (*22*). One experiment was also conducted with a maximum viscosity cutoff and a 300-K surface temperature, yielding very similar results.

The background viscosity in the upper mantle η_{ref} was 6 $\times$ 10^{20} Pa·s, which is the value at T_{ref} = 1700 K and D = 400 km (Table 1). The Rayleigh number based on this viscosity was 10^5. Viscosities as high as 3 $\times$ 10^{24} Pa·s and as low as 6 $\times$ 10^{17} Pa·s were achieved when A = 15 for a total viscosity contrast of 5 $\times$ 10^6.

We explored the sensitivity of the model results to variations in T_p and the constant A in Eq. 1 that determines the temperature sensitivity of the mantle's viscosity. Measurements of A for the mantle ranged from 30 to 40 (*23*). The temperature required for a 1/*e* change in viscosity defines a rheological temperature scale ΔT_{rheol}, given by (*10*)

$$\Delta T_{rheol} = \left|\frac{\eta}{d\eta/dT}\right| \quad (3)$$

This scale, which is about 50 K in the Earth's mantle, has multiple roles to play in controlling lithospheric thinning.

Lithospheric thinning is a two-step process. First, the plume spreads when it can no longer rise through the viscous lithosphere. This spreading is accomplished by displacement of lithospheric material that is not more than a few times more viscous (not more than ΔT_{rheol} cooler) than the normal asthenosphere. The volume of this material is proportional to ΔT_{rheol}, and its associated buoyancy flux is proportional to ΔT^2_{rheol}. Because of the inverse dependence on A, mechanical thinning is not likely to remove much material in the Earth's mantle, as demonstrated by previous numerical models in which it was the only available mechanism for thinning (*16*, *17*).

Laboratory results (*9*, *10*) have shown that increasing A leads to more vigorous small-scale convection. We obtained a similar effect by increasing the plume temperature T_p. These small-scale instabilities are the second step in lithospheric thinning (*6*, *7*).

The onset of small-scale convective modes with three different solutions for A = 15 (total viscosity contrast 10^6) and increasing values of T_p is shown in Fig. 2. The 3D isotherms shown are one-quarter T_p above the background mantle temperature.

The interaction of the lowermost lithosphere with the spreading plume material is different in each snapshot in Fig. 2. When small-scale modes are not present, the plume is in a steady regime. This regime is obtained at low T_p or A (or low values of both). Most previous numerical studies (*16*,

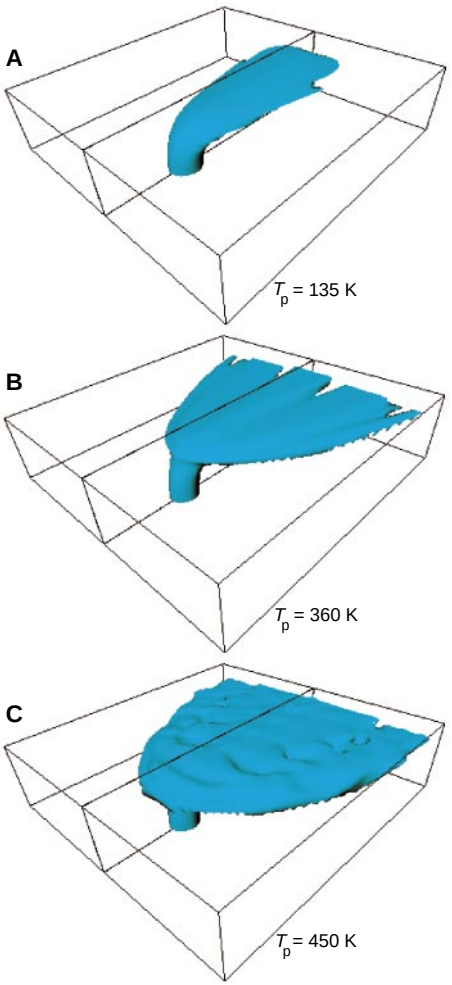

Fig. 2. One-quarter T_p isothermal surfaces from models with A = 15 and T_p = (**A**) 135 K, (**B**) 360 K, and (**C**) 450 K. The patterns in (A) and (B) are steady; the pattern in (C) is highly time-dependent. The model domain is reflected about the plume's center line.

Table 1. Model parameters and values.

Parameter	Symbol	Value
Depth of domain	D	400 km
Gravitational acceleration	g	9.8 m s^{-2}
Thermal expansivity	α	3.1 $\times$ 10^{-5} K^{-1}
Thermal diffusivity	κ	10^{-6} m^2 s^{-1}
Reference density	ρ_0	3400 kg m^{-3}
Reference temperature	T_{ref}	1700 K
Surface temperature	T_{surf}	800 K
Temperature drop	$\Delta T = T_{ref} - T_{surf}$	1400 K
Reference viscosity	η_{ref}	6 $\times$ 10^{20} Pa·s
Rayleigh number	$Ra = \frac{\rho_0 g \alpha \Delta T D^3}{\eta_{ref}\kappa}$	9.3 $\times$ 10^4

17) fall into this regime. Conduction controls the heat transfer into the lithosphere, which does not warm substantially before exiting the computational domain (dotted line in Fig. 3).

Small-scale modes first appear as rolls aligned with the plate motion. This shear-aligned roll regime is illustrated in Fig. 2B. It occurs when T_p is between 200 and 400 K for $A = 15$. The lowermost lithosphere descends through the plume material in several sheets aligned with the plate motion, which appear as notches in the fan of plume material in Fig. 2B. This action increases the heat transfer into the lithosphere as seen in the center line temperature profile (dashed line in Fig. 3). A similar solution was obtained in a previous study with only depth-dependent viscosity (*24*). These rolls are similar in character to Richter rolls (*25*) and occur in an active sublayer with a temperature difference of a few times ΔT_{rheol}.

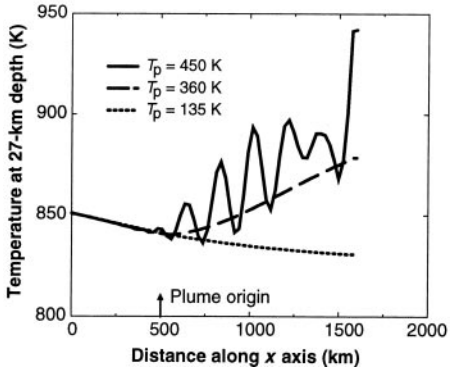

Fig. 3. Temperatures 27 km below the top of the domain (60-km depth) along the axis of the plume for the cases shown in Fig. 2. The plume origin is indicated by the arrow, 500 km from the upstream boundary.

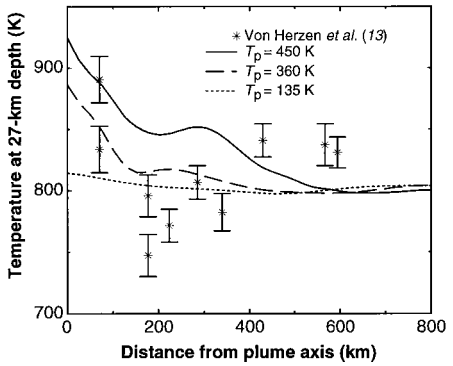

Fig. 4. Temperatures 27 km below the top of the domain (60-km depth) perpendicular to the axis of the swell for the cases shown in Fig. 2. The profiles are taken 1100 km downstream of the plume origin. Temperatures extrapolated from the heat flow measurements of (*13*) are plotted as asterisks with 1σ errors.

The third regime is unsteady, and the snapshot in Fig. 2C is representative of a time-dependent pattern. This regime occurs for high T_p or A (or high values of both), when the shear-aligned rolls become unstable to 3D perturbations (*26*). The resulting pattern is a complex and time-dependent combination of downwelling sheets and drips (Fig. 2C). The heat transfer into the lithosphere is substantially enhanced over the steady regime (solid line in Fig. 3).

Temperature profiles perpendicular to the swell 27 km below the top of the domain (60 km deep) are shown in Fig. 4, 1100 km downstream of the plume origin. The profile extends 800 km from the swell axis. The steady, low-T_p case (dotted line) shows a small and smooth increase in the temperatures from the edge of the plume at ~500 km all the way up to the swell axis. The moderate-T_p case in the shear-aligned roll regime (dashed line) shows a greater temperature increase than the conductive regime and is no longer monotonic. The downwelling branch of the roll located ~200 km from the plume axis depresses temperatures in the lithosphere above it, creating a dip in the temperature profile. This pattern is similar in shape, if not amplitude, to the temperatures at this depth extrapolated from heat flow observations (*13*), plotted as asterisks with 1σ error bars. In the unsteady regime at high T_p (solid line in Fig. 4), the lithospheric temperature increase is greater but more variable across the swell, with undulations on smaller scales than in the moderate-T_p case. Surface heat flow variations of 10 to 20% result for the moderate-T_p case, increasing to 60% for the high-T_p case. If the variation in the heat flow measurements is not the result of near surface effects, then they may indicate the presence of small-scale modes.

Mechanical thinning does contribute an important feature of the convection. A downwelling curtain forms at the edge of the spreading plume material (Fig. 5), ultimately isolating it from the rest of the mantle. This curtain is a feature of the convection in every case, arising through the mechanical displacement of the lowermost lithosphere. Some of the plume material is entrained by this downwelling and exits the box at the base, although most of it exits the box in the direction of plate motion. This curtain does not break up into cylindrical downwellings within the 400-km depth of the computational domain, although it may at greater depths. As long as the curtain remains intact, which it does for at least 1000 km downstream, the plume material cannot mix with the rest of the mantle and remains isolated until it becomes part of the lithosphere or is entrained into the large-scale downwelling at a subduction zone. Substantial lateral geochemical heterogeneity should result from this process.

Our experiments have shown that for a more temperature-dependent viscosity (higher A), the transition to quasi-steady rolls occurs at lower T_p. The transition to unsteady, 3D convection has not been mapped, but it may show similar behavior because it is observed when $A = 15$, but not when $A = 12$, at the same T_p. Using the rheological temperature scale to nondimensionalize T_p, we found that the shear-aligned roll regime occurs at $T_p/\Delta T_{rheol}$ between 2 and 3, independent of A. This finding allows us to extrapolate from our low-A experiments to the Earth's mantle, where ΔT_{rheol} is around 50 K. Thus, plumes with peak excess temperatures between 100 and 150 K fall into the shear-aligned roll regime. Hotter plumes exhibit time-dependent, 3D instabilities, although the roll pattern is still evident in the near-surface temperatures (solid line in Fig. 4) and consequent surface heat flow anomaly.

The fit to the heat flow data made in this report should not be considered quantitative but merely suggestive. We did not attempt to optimize the fit in any way. The very broad scale of variation is probably not achievable without widening our computational domain. It should be emphasized that only one sparsely sampled heat flow line was surveyed at the Hawaiian swell and that near surface effects could be responsible for the observed variation.

The other data available for comparison are the geoid and topography fields, conveniently expressed in terms of the dimensionless geoid-topography ratio (GTR). The GTR for the Hawaiian swell is about 0.01.

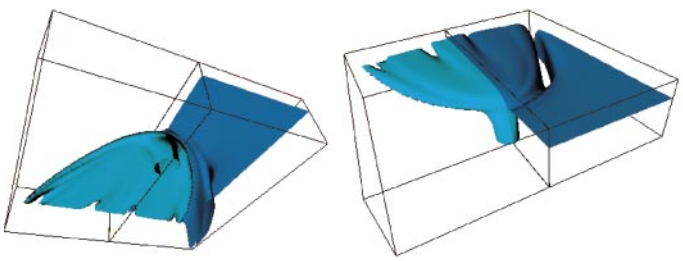

Fig. 5. Two views of two isotherms showing the plume (aqua, $T = 2060$ K) and the downwelling curtain (blue, $T = 1655$ K) that surrounds it. $T_p = 360$ K and $A = 15$ for this case, which is also shown in Fig. 2B.

The results of our numerical experiments give values from three to ten times this value. Some of this difference is due to the lack of deeper mantle flow, and some of it is due to the weakness of the temperature dependence (our highest A is still about a factor of two too small), which creates a strong downwelling curtain leading to large negative topography and geoid. This curtain is the result of mechanical thinning and would be much smaller at Earth-like values of A.

The range of buoyancy fluxes in our experiments (calculated from the rate at which topography is created) is 0.8 to 10.7×10^6 g s^{-1}, which includes the estimated value for the Hawaiian swell. As demonstrated in (*17*), the plume buoyancy flux is smaller than the buoyancy flux measured from the topography, because of the buoyancy flux of the downwelling curtain. The buoyancy flux does not obey a simple scaling with either A or T_p, because of competition between mechanical thinning, spreading of plume material within the asthenosphere, and thinning by small-scale instabilities. Experiments to control these factors individually should be designed.

We have demonstrated that the small-scale instabilities that promote lithospheric thinning are initiated when the excess temperature of the plume is about twice ΔT_{rheol}, independent of A. This finding gives us confidence in extrapolating to Earth-like values of A, which require only modest plume temperatures ($T_p > 100$ K) to produce small-scale convective flows.

REFERENCES AND NOTES

1. R. S. Dietz and H. W. Menard, *J. Geol*. **61**, 99 (1953).
2. S. T. Crough and G. A. Thompson, *Earth Planet. Sci. Lett*. **31**, 397 (1976).
3. R. S. Detrick and S. T. Crough, *J. Geophys. Res*. **83**, 1236 (1978).
4. S. T. Crough, *Geophys. J. R. Astron. Soc*. **55**, 451 (1978).
5. D. T. Sandwell, *J. Geophys. Res*. **87**, 1001 (1982); T. Spohn and G. Schubert, *Tectonophysics* **94**, 67 (1983); A. O. Gliko, *Izvest. Acad. Sci. USSR* **22**, 257 (1986); G. M. Liu and C. G. Chase, *J. Geophys. Res*. **94**, 5571 (1989).
6. L. Fleitout, C. Froidevaux, D. Yuen, *Tectonophysics* **132**, 271 (1986).
7. L. Fleitout and D. A. Yuen, *J. Geophys. Res*. **89**, 9227 (1984); D. A. Yuen and L. Fleitout, *Nature* **313**, 125 (1985).
8. R. W. Griffiths and I. H. Campbell, *J. Geophys. Res*. **96**, 18295 (1991).
9. H. C. Nataf and F. M. Richter, *Phys. Earth Planet. Inter*. **29**, 320 (1982); F. M. Richter, H. C. Nataf, S. F. Daly, *J. Fluid Mech*. **129**, 173 (1983); A. Davaille and C. Jaupart, *J. Geophys. Res*. **99**, 19853 (1994).
10. ———, *J. Fluid Mech*. **253**, 141 (1993).
11. S. Morris and D. Canright, *Phys. Earth Planet. Inter*. **36**, 35 (1984); A. C. Fowler, *Stud. Appl. Math.* **72**, 189 (1985); E. F. Fishbein, thesis, University of California, Los Angeles (1988).
12. R. P. Von Herzen *et al*., *J. Geophys. Res*. **87**, 6711 (1982).
13. R. P. Von Herzen, M. J. Cordery, R. S. Detrick, C. Fang, *ibid.* **94**, 13783 (1989).
14. N. H. Sleep, *ibid.* **99**, 9327 (1994); J. Phipps-Morgan, W. J. Morgan, E. Price, *ibid.* **100**, 8045 (1995); N. M. Ribe, *ibid.* **101**, 16195 (1996); N. H. Sleep, *ibid.*, p. 28065.
15. M. T. Woods and E. A. Okal, *Geophys. J. Int*. **125**, 325 (1996).
16. M. Monnereau, M. Rabinowicz, E. Arquis, *J. Geophys. Res*. **98**, 809 (1993).
17. N. M. Ribe and U. R. Christensen, *ibid.* **99**, 669 (1994).
18. P. J. Tackley, thesis, California Institute of Technology, Pasadena (1994); *J. Geophys. Res*. **101**, 3311 (1996).
19. G. F. Davies, *J. Geophys. Res.* **93**, 10467 (1988); N. H. Sleep, *ibid.* **95**, 6715 (1990).
20. E. M. Robinson, B. Parsons, S. F. Daly, *Earth Planet. Sci. Lett*. **82**, 335 (1987); E. M. Robinson and B. Parsons, *J. Geophys. Res*. **93**, 3469 (1988).
21. E. Takahashi, *J. Geophys. Res.* **91**, 9367 (1986); F. J. Zhang and C. Herzberg, *ibid.* **99**, 17729 (1994).
22. J. G. Caldwell and D. L. Turcotte, *ibid.* **84**, 7572 (1979).
23. R. S. Borch and H. W. Green, *Phys. Earth Planet. Inter*. **55**, 269 (1989).
24. P. E. van Keken and C. W. Gable, *J. Geophys. Res*. **100**, 20291 (1995).
25. F. M. Richter, *ibid.* **78**, 8735 (1973).
26. F. H. Busse and J. A. Whitehead, *J. Fluid Mech*. **47**, 305 (1971).

27. We thank the three reviewers for their insightful comments. This research was partially funded by NASA grants NAG54628 and NAG53863.

14 October 1997; accepted 12 January 1997

Photometry and Spectroscopy of the GRB 970508 Optical Counterpart

Alberto J. Castro-Tirado, Javier Gorosabel, Narciso Benítez, Christian Wolf, Ralf Fockenbrock, Enrique Martínez-González, Helmuth Kristen, Adrick Broeils, Holger Pedersen, Jochen Greiner, Enrico Costa, Marco Feroci, Luigi Piro, Filippo Frontera, Luciano Nicastro, Eliana Palazzi, Corrado Bartolini, Adriano Guarnieri, Nicola Masetti, Adalberto Piccioni, Marco Mignoli, Magrethe Wold, Mark Lacy, Kurt Birkle, Tom Broadhurst, Søren Brandt, Niels Lund

An optical transient within the error box of the gamma ray burst GRB 970508 was imaged 4 hours after the event. It displayed a strong ultraviolet excess, and reached maximum brightness 2 days later. The optical spectra did not show any emission lines, and no variations on time scales of minutes were observed for 1 hour during the decline phase. According to the fireball and afterglow models, the intensity should rise monotonically before the observed optical maximum, but the data indicate that another physical mechanism may be responsible for the constant phase seen during the first hours after the burst.

Gamma ray bursts (GRBs), brief flashes of cosmic high-energy photons, remain one of the most elusive mysteries for high-energy astrophysicists (*1*), mainly because we do not know how far away they are. The finding of counterparts—transient emissions released at other wavelengths after the bursts—is needed to help explain their origin. Since the advent of the Italian-Dutch x-ray satellite BeppoSAX in April 1996 (*2*), it has been possible to perform deep multiwavelength searches just a few hours after an event, allowing the detection of counterparts associated with the GRBs.

On 8 May 1997, 21:41:45 UT, GRB 970508 was detected by the gamma ray burst monitor (*3*) and the wide-field camera (*4*) of BeppoSAX. The single-peaked GRB lasted 15 s, and its position (*5*) was further refined to a radius of 3 arc min (*6*). This event was also observed as a rather weak GRB by the Burst and Transient Source Experiment (BATSE) on the Compton Gamma-Ray Observatory. The duration was about 35 s, with a single main pulse lasting 3.6 s, reaching a peak flux (50 to 300 keV) of $\sim 2 \times 10^{-10}$ J m^{-2} s^{-1}. The gamma ray fluence (flux integrated over time) was $\sim 1.6 \times 10^{-9}$ J m^{-2} (*7*). After 5.7 hours, BeppoSAX was reoriented toward the burst location, and an x-ray source was detected within the region of uncertainty given by the less accurate GRB localization (the error box) (*8*).

We obtained unfiltered and R-band images with the Calar Alto Faint Object Spectrograph at the 2.2-m telescope of the German-Spanish Calar Alto Observatory (CAHA), beginning 4 hours and 6 min after the GRB (9 May, 1:48 UT). The 2048 × 2048 pixel charge-coupled device (CCD) frames with scale 0.53 arc sec per pixel provided a circular field (16 arc min in diameter), which was centered on the initial GRB location. We also obtained a mosaic of images with the 4.2-m William Herschel Telescope (WHT) on La Palma (Canary Islands), starting 4 hours and 24 min after the event. The position of the x-ray source was imaged (300-s exposure) by the